CrossMark

A Comparative Study on Interlaminar Properties of L-shaped Two-Dimensional (2D) and Three-Dimensional (3D) Woven Composites

Qiaole Hu[1,2] · Yihui Zhang[1,2] · Yanyun Mao[1,2] · Hafeezullah Memon[1,2] · Yiping Qiu[1] · Yi Wei[1,2] · Wanshuang Liu[1,2]

Abstract

The effect of fiber-resin interfacial structures (especially three-dimensional (3D) structures) on the delamination resistance of L-shaped beam composites was investigated via hinged loading tensile tests. Four types of structures were woven, and the corresponding reinforced epoxy composites were manufactured through a vacuum-assisted resin infusion (VARI) process. The results revealed that the two-dimensional (2D) laminate and 3D shallow-straight woven composite (3DSSWC) had the similar interlaminar strength and failed via delamination. However, compared with the resistance of these composites, a significantly higher delamination resistance was realized for a 3D orthogonal woven composite (3DOWC) and a 3D shallow-bend woven composite (3DSBWC). This high resistance resulted from the reinforcing fibers (i.e., Z-yarns) in the Z-direction and the considerable yarn waviness of the 3DOWC and the 3DSBWC, respectively. The failure mode of 3DOWC was characterized by interlayer delamination and Z-yarn or weft yarn breakage. Moreover, the failure mode of 3DSBWC was dominated by delamination and weft yarn breakage. Therefore, the 3D orthogonal (3DOW) and 3D shallow-bend (3DSBW) woven structures were quite effective in resisting delamination and, of the structures considered, the 3DSBW structure yielded the best L-shaped beam composite.

Keywords 3D woven composite · L-shaped beam · Carbon fibers · Mechanical properties

✉ Yi Wei
weiy@dhu.edu.cn

✉ Wanshuang Liu
wsliu@dhu.edu.cn

[1] Key Laboratory of Textile Science &Technology, Ministry of Education, College of Textiles, Donghua University, 2999 North Renmin Road, Shanghai 201620, China

[2] Donghua University Center for Civil Aviation Composites, Donghua University, 2999 North Renmin Road, Shanghai 201620, China

🍀 Springer

1 Introduction

Since the invention of composite materials, two-dimensional (2D) laminates, i.e., the primary form of laminates, have been widely used for aerospace, rail, automobiles and construction application [1, 2]. These applications fully exploit the excellent mechanical properties, as well as weight-reduction characteristics, and manufacturing efficiency of the laminates. However, the poor interlaminar strength of this materials, limits their ability to bear the transverse load. This limitation is particularly profound for composite structures having curved shapes, such as the ribs and stringers shown in Fig. 1. When these structures are subjected to normal end loading, a shear or radial tensile stress is generated in the through-thickness direction (Z-direction), especially in regions where high bending moments occur, thereby leading to delamination failure. In contrast to 2D laminates, the two-dimensional (3D) woven composites consist of continuous fibers aligned in the Z-direction. These fibers are either direct reinforcing yarns (i.e., Z-yarns) or warp yarns that interlock layers of weft yarns. Therefore, compared with 2D composites, the 3D composites will probably provide better load bearing in the Z-direction, as well as higher resistance to delamination [3–9].

With increasing use of composite materials as primary structures, the ability to understand and predict the interlaminar properties and failure modes (especially of curve-shaped beams) has become critical.

The interlaminar shear strength and failure mode of curved composite beams were first studied in the 1990s. Two types of curved beam specimens (semicircular and elliptical) were subjected to static and fatigue loads and the corresponding through-thickness properties were
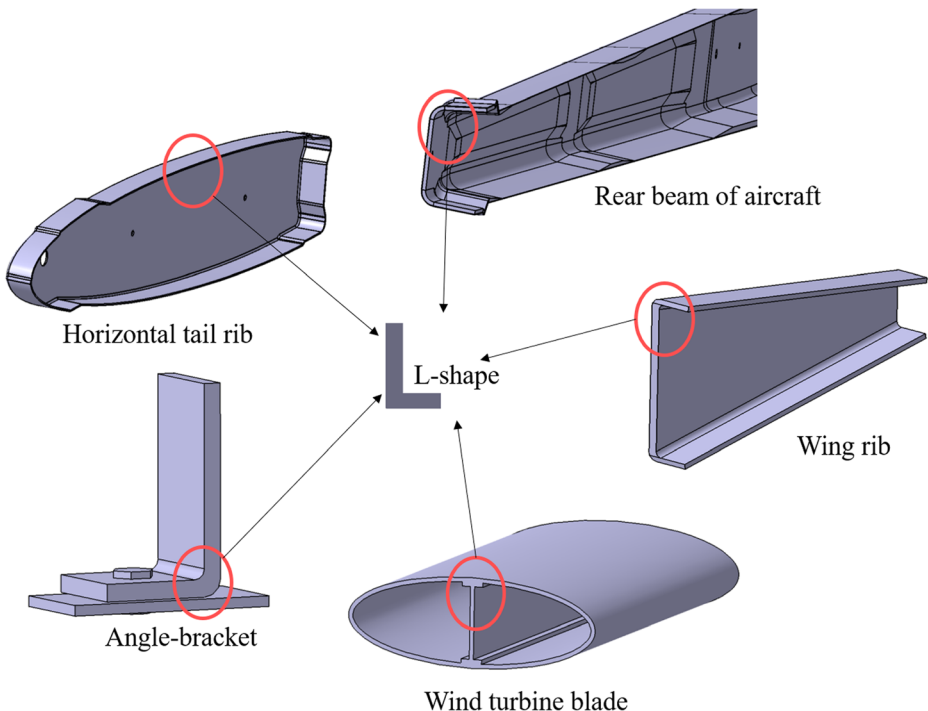

Fig. 1 Schematics of typical curved structures

measured [10]. The results revealed that the quality of the laminate was poor, as evidenced by a high void content, and high thickness variations in the case of the semi-circular beams, resulted in poor mechanical property. However, the in-plane transverse strength of the elliptical beams was almost twice that of the semi-circular beams. Martin et al. [11, 12] analyzed the delamination in L-shaped cross-ply and unidirectional laminate composites under perpendicular loading to the arm (Fig. 2a). The experimental and numerical analysis showed that delamination was initiated in the bending area, where the radial stress was highest. Moreover, as determined via finite element analysis (FEA), the energy released during delamination propagated into the arms of the laminates. The geometry (i.e., width, loading arm length, inner radius and thickness) of the L-shaped beams was varied and the interlaminar tensile strength was determined [16]. The results revealed that the specimen width and loading arm length had little effect on the Z-direction properties, but the effect of thickness and inner radius was inconclusive due to poor laminate quality. In 2009, this issue was revisited by Wimmer et al. [17], who investigated (via experiments and simulations) the occurrence of initial delamination and the growth of existing delamination in unidirectional L-shape laminates. The experimental results corresponded closely with those of the computational models using the Virtual Crack Closure Technique (VCCT). The results revealed stable crack growth for a 3-mm pre-crack and unstable crack growth for specimens without initial delamination. In addition, Gozluklu and Coker [13] used FEA in conjunction with cohesive zone methods to investigate the
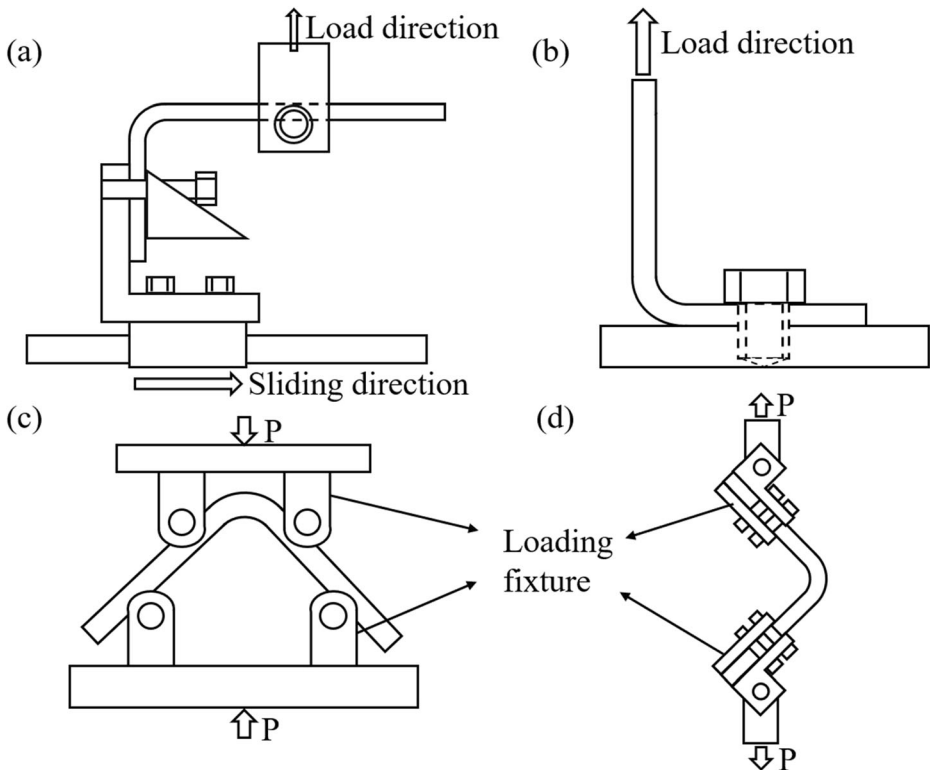

Fig. 2 Test design of the L-shaped curved beam a perpendicular [11, 12], b parallel to the arm loading [13], c four-point bending and d hinged loading tensile test [14, 15]

dynamic delamination process in L-shaped beams with a 1-mm pre-crack under parallel loading (Fig. 2b). The simulations revealed that the crack tip speed reaches 800 m/s under the shear- dominated mode, and unstable delamination occurred under a mix-mode stress state, where a secondary crack nucleated at the arm. In subsequent work, they investigated the effect of pre-crack length on the stability of crack propagation in unidirectional L-shaped composite laminates [18]. The experimental results corresponded closely to the FEA results, i.e., unstable dynamic crack growth was observed for a small (14 mm) pre-crack, whereas stable crack propagation occurred for a large (60 mm) pre-crack. In the same year, Coker et al. [19, 20] investigated dynamic delamination in L-shaped composite beams under quasi-static loading perpendicular to one arm. The experimental and FEA analysis with a bilinear cohesive zone model revealed that the crack tip speeds transitioned from sub-Rayleigh to intersonic as the crack propagated from the curved region to the arms. Most recently, Coker et al. [21, 22] found that the failure mechanism varies with the lay-up sequence.

However, the abovementioned studies focused on 2D laminates, and curved beams fabricated from 3D woven fabrics were only considered in a few cases. Jackson [14, 15] used the four-point bending and hinged loading tensile test (Fig. 2c and d) to characterize the through-thickness properties of various composites (i.e., 2D and 3D braids, prepreg tapes, 2D and 3D weaves). The results revealed significantly different failure modes between 2D and 3D composites. The study showed that interlayer delamination in the 2D composites resulted from the out-of-plane stress. In contrast, the failures of 3D materials were attributed to the radial cracks induced by high circumferential stresses along the inner radius. In 2014, the behavior characterizing L-shaped beams of 2D non-woven carbon fabric (NCF) and 3D woven composites was investigated via four-point bending test [23]. The results demonstrated that, compared with the 2D composites, the 3D woven composites could bear more than twice the load, and could carry the load after initial failure.

In this study, an L-shaped beam was selected, as this is the most basic and frequently encountered geometry in composite parts, especially for stiffeners such as I, C, T, and Z beams. The failure mode of such 3D composite structures remains poorly understood. Therefore, a systematic study focusing on the failure mode will be beneficial for both the design and use of these essential load-bearing parts. L-shaped beam composites composed of four types of woven fabrics (i.e., 2D, 3DOW, 3DSBW and 3DSSW) were investigated using hinged loading tensile tests. The effect of these woven structures on the failure modes was investigated via an optical microscope and X-ray computed tomography (X-CT). Results generated herein can serve as a design parameter for predicting the failure process via finite element modeling.

2 Experimental Details

2.1 Sample Preparation

The effect of fabric structures on the interlaminar shear strength was determined for four different fiber architectures. The carbon fibers (i.e., SYT55S-12) and the preforms were obtained from Zhongfu Shenying Carbon Fiber Co., Ltd. (China) and Huaheng High Performance Fiber Textile Co., Ltd. (China), respectively. Considering the weaving condition and structure effect, these four structures were fabricated along warp/X direction. A schematic of the four structures used to fabricate the L-shaped beam composite beams is shown in Fig. 3a–d.
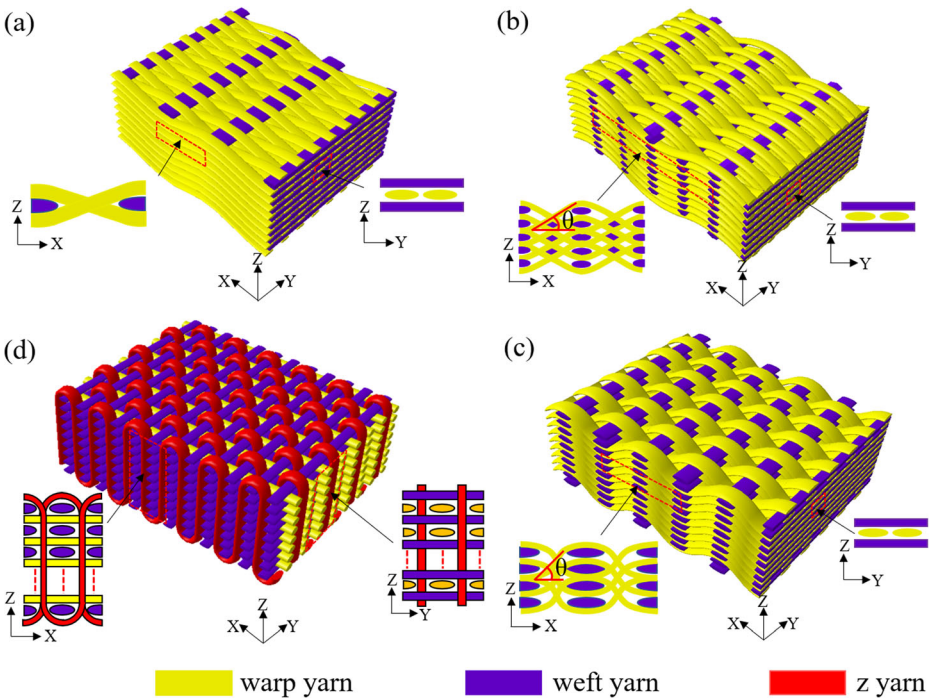
Fig. 3 Schematics of 2D (**a**), 3DSSW (**b**), 3DOW (**c**) and 3DSBW (**d**) woven fabrics

As showed in Fig. 3a, the 2D construction is composed of two types of yarn systems (i.e. warp and weft yarns) and the warp yarn is woven repetitively over and under the weft yarns, which was called plain weaving structure in textile field.

The 3D Layer-to-Layer fabric, named 3D shallow-straight woven structure (3DSSW) and 3D shallow-bend woven structure (3DSBW) in Fig. 3b and c, which also only contain two sets of yarns (i.e. warp and weft yarns), but the warp yarns were placed at an angle, θ, to the thickness direction to hold the non-crimp weft yarns together. For 3DSSW fabric with eight warp layers and eight weft layers, the warp yarn is interwoven with only one layer of weft yarn in the thickness direction (Z-direction) while weaving one weft interval length in the longitudinal direction (X-direction). However, for 3DSBW fabric with eight warp layers and nine weft layers, a warp yarn interlaces two adjacent weft layers in the Z-direction.

For the 3D orthogonal woven (3DOW) construction, the fabric was woven with an orthogonal fiber structure that consisted of in-plane non-crimp warp and weft yarns interlaced

Table 1 Weaving parameters of the fabrics

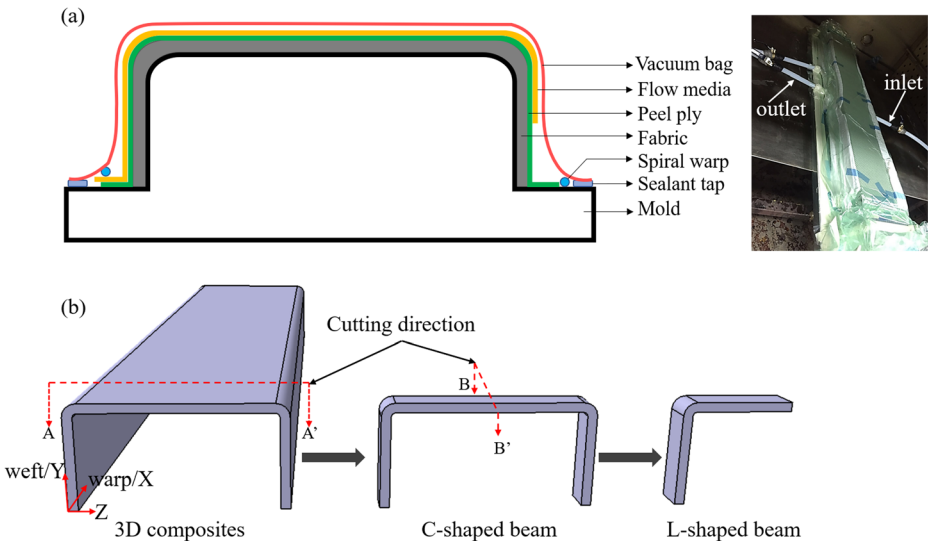|	2D	3DSS	3DSB	3DO
Linear density (tex)	450			
Yarn density (ends/cm)	warp:3.4	warp: 9	warp: 9	warp(z): 9
	weft:3.2	weft: 3	weft: 3	weft: 3
Thickness (mm)	2.72	5.40	5.20	7.00
Layers (warp×weft)	8 × 8	8 × 8	8 × 9	8 × 9
FVF of fabric (%)	/	47.3	47.4	47.7

Fig. 4 **a** Illustration of VARI process lay-up **b** L-shaped beam preparation method

in the through-thickness direction with the Z binder yarns, showed in Fig. 3d. The corresponding weaving parameters are listed in Table 1.

The 2D laminate and 3D composites were fabricated via a vacuum assisted resin infusion (VARI) process, as shown in Fig. 4a. An epoxy resin (BAC 172; supplied by Zhejiang Baihe Advanced Composites Ltd.) was used as the composite matrix. A resin infusion temperature of 30 ± 2 °C was maintained during the process and curing was performed in the oven at 120 °C for 1 h. Using a high-pressure water jet, the composites were cut along the weft direction (A-A') to obtain the C-shape samples and then cut along the warp direction (B-B′) to obtain the L-shape tension test samples, (see Fig. 4b). A fiber volume fraction of $54 \pm 2\%$ was maintained for each composite sample was controlled.

2.2 Tensile Test

A schematic of the L-shape specimens is shown schematically in Fig. 5. The test parameters, i.e., the loading arm length L, width w, thickness t, and inner radius R_i (all in mm), for each composite are listed in Table 2. The quasi-static tension test was performed at a crosshead speed of 1 mm/min on an LD26-5105 tester (Labscans, China, 10KN load cell). The load was applied via a hinged steel loading fixture, shown in Fig. 5a and b. To clearly observe the location of the first crack and the propagation path of the cracks, the edges of the specimen were painted white with a water-resistant paint and the dynamic process was captured by a USB digital microscope (UM012C, see Fig. 5b).

2.3 Micro X-CT Measurements

Three-dimensional images of the cracks inside the L-shape coupons after tension failure were obtained via Micro X-CT (diondo d2), a non-destructive X-ray perspective technique. These measurements were aimed at obtaining information on crack propagation inside the specimens, and were performed at the same spatial resolution (i.e., 7 μm) of the X-CT for all samples. The
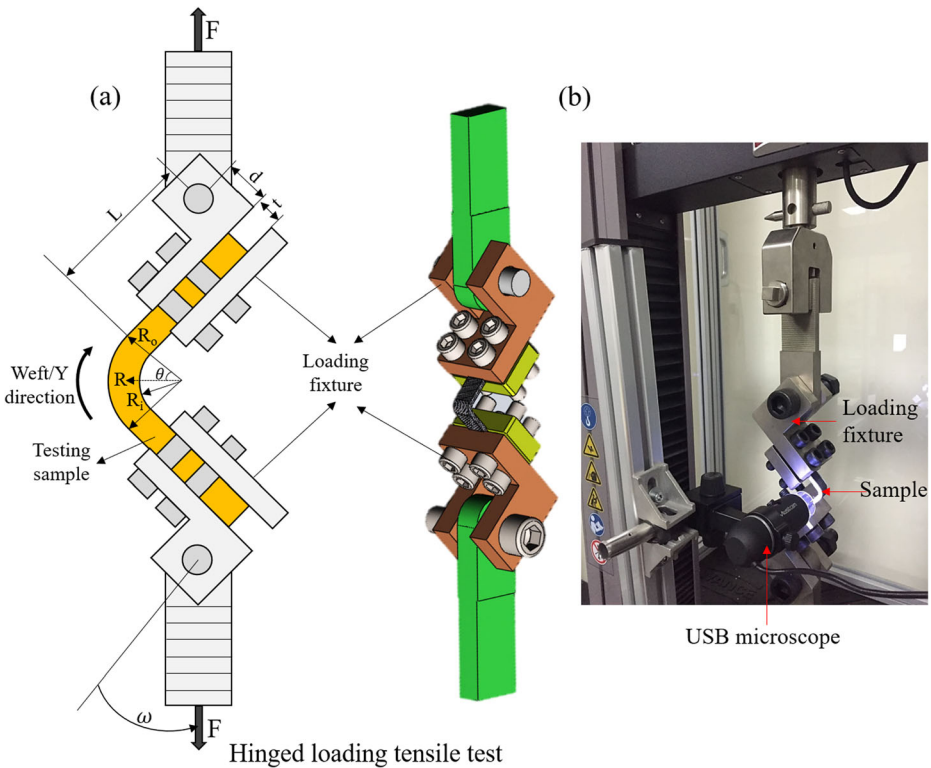
Fig. 5 Tensile test design for the L-shaped beam **a** hinged loading device **b** L-shape tensile test

X-ray CT apparatus consists of three devices: the X-ray source, a detector, and a rotating geometry (see Fig. 6). During the measurements, the samples underwent a 360° rotation and the X-rays penetrated the specimen through a single shaft. Based on the different absorption and transmittance of the rays in the composites, radiographs were obtained during the rotation and were reconstructed (using a computer) into 3D tomography images.

3 Results and Discussion

3.1 Morphology of the L-shape Cross-Section

In fiber reinforced composites, the fiber constitutes the primary load bearing party, especially under tension. As a result, the degree of fiber buckling has considerable effect on the

Table 2 Parameters of the L-shaped beam composites

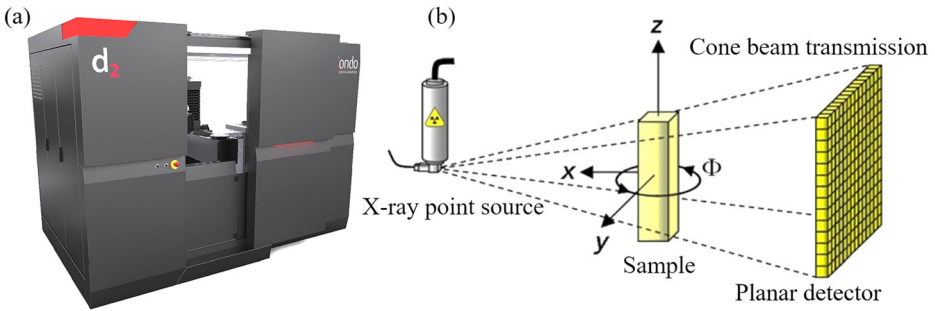| Structures	L	R_0	R	R_i	w	t	d
2D	89.1	6.3	5.1	4	14.6	2.3	48.2
3DSSW	87.3	7.9	5.9	4	15.6	3.9	48.2
3DSBW	86.5	8.3	6.2	4	15.5	4.3	48.2
3DOW	85.8	10.3	7.2	4	15.3	6.3	48.2

Fig. 6 X-ray CT apparatus used for non-destructive damage detection of L-shaped tension samples **a** testing machine and **b** test philosophy of X-ray CT

mechanical properties. Fiber buckling is largely determined by the weaving or braiding method employed. Therefore, an understanding of the topology is essential for determining the effect of the structures on the performance and failure of the parts under loading.

3.1.1 Morphology along the A-A′ Section

The cross-sections of the four composites along the A-A' direction are shown in Fig. 7a. As the figure shows, the warp yarns (X-direction) in the 2D laminate, 3DSSWC, and 3DSBWC were all characterized by sinusoidal shapes, whereas the warp yarns in 3DOWC were linear. In addition, these composites could be ranked in ascending order of warp yarn waviness, i.e., 3DOWC < 2D laminate≤3DSSWC < 3DSBWC. Owing to the yarn interlacing style and yarn flattening during the VARI process, the yarn waviness of 3DSSWC was similar to that of the 2D laminates.

The cross-sections of weft yarns in the A-A' section differed in this group. Lenticularly shaped yarns occurred in 2D laminate, 3DSSWC, and 3DSBWC. This was attributed to the void/gap condensation among the fibers and the yarn cross-section deformation, resulting from compression during the VARI process. In addition, yarn nesting or slipping during the process resulted in a certain Z-direction inclination of the weft yarn cross-section.

However, the cross-section of weft yarns in 3DOWC was characterized by an elliptical shape with variable dimensions along the Z-direction. This was attributed to squeezing of these yarns by the adjacent warp yarns and Z-yarns that resulted in differing degrees of yarn cross-section deformation. Moreover, after the VARI process, the Z-yarn path changed from the U shape to the familiar trapezoid shape.

3.1.2 Morphology along the B-B′ Section

Figure 7b shows the cross-section along the weft/Y direction. The straight weft yarns occurred in all four composites. This may have resulted from the yarn flattening (during the VARI process) that resulted in a slight reduction of the waviness and, in turn, lessening of weft yarn crimping.

The cross-sectional shape of warp yarns in the B-B′ section differed significantly among these composites. This was attributed to differing deformation mode of the yarn cross-section. For example, in the 2D composite, the warp yarns were squeezed by the crossed weft yarns, resulting in lenticular-shaped cross-sections of the warp yarns. However, the warp yarns in the
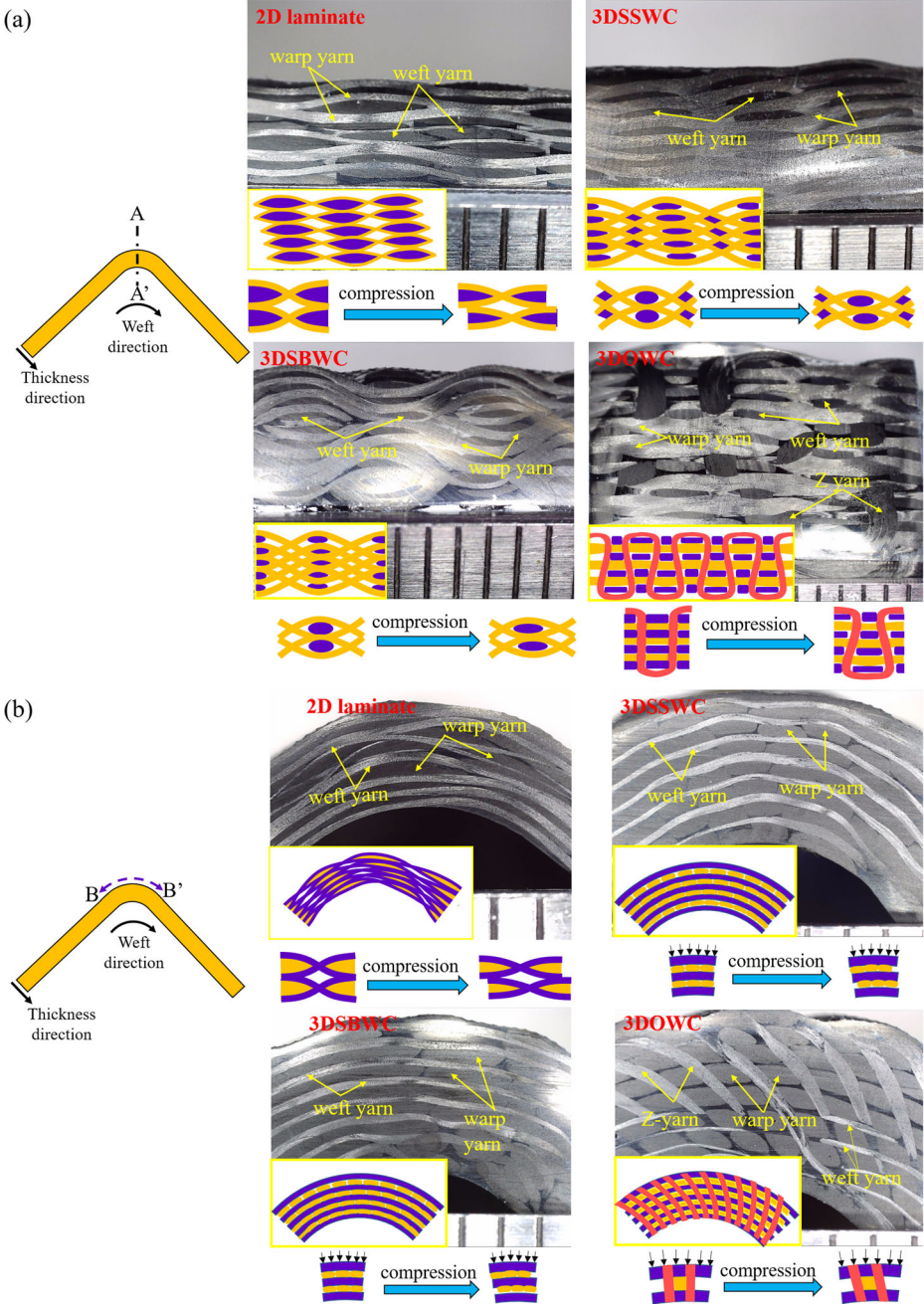
Fig. 7 Cross section of L-shaped composites (2D laminate, 3DSSWC, 3DSBWC, 3DOWC) along the **a** A-A' and **b** B-B' direction

3DSSWC and 3DSBWC were only compressed by the parallel weft yarns, resulting in racetrack-shaped cross-sections of these yarns. The warp yarns in 3DOWC underwent

compression by the parallel weft yarns, and experienced the limiting effect of the Z-yarns. This resulted in a parallelogram-like the cross-sectional shape of these yarns.

In addition, the inclination of the warp yarn cross-section with respect to the Z-direction, resulted mainly from the combined effect of bending, yarn nesting and slipping accompanying yarn compression during the VARI process. Moreover, an uneven yarn thickness along the path direction was observed for these composites. This was again attributed to the yarn bending deformation associated with the VARI process.

In conclusion, the factors affecting the compaction behavior of these woven fabric preforms during the VARI process were as follows: yarn nesting and slipping, void/gap condensation, yarn cross-section deformation, tow flattening and bending, as previously reported for the 2D laminates [24–29]. Furthermore, based on the morphology of the L-shape cross-section, the yarn cross-section and path may exert significant influence on the load transfer during the L-shape test and (on) the final failure mode.

3.2 Tensile Test

The load-displacement curves of the four L-shape composite beams are shown in Fig. 8. For 2D laminate and 3DSSWC, sharp load drops occurred upon crack initiation, and the coupon failed immediately afterward. For the 3DSSW, the load occurred at nearly 50% attenuation and then fluctuated for a short while without an immediate drop in the subsequent loading. The difference in deformation behavior may have resulted from the higher degree of yarn crimp in the 3DSSWC (compared with that of the 2D laminates).
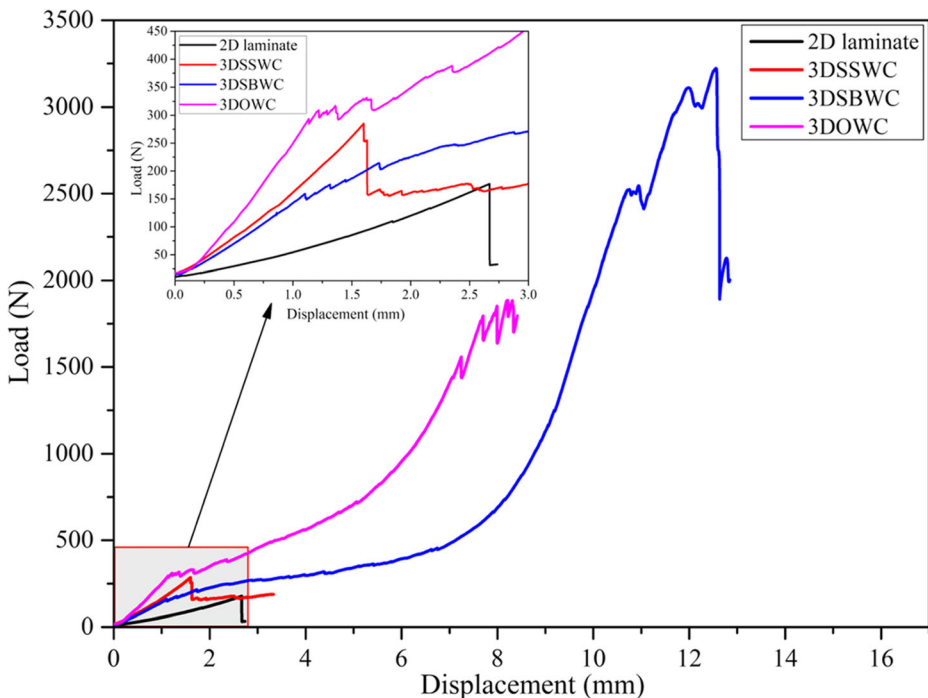

Fig. 8 Load-displacement curve of the L-shaped composites

However, 3DOWC and 3DSBWC exhibited multi-stage failure during the entire loading process and both had a transitional region at 2–7 mm. This may have resulted from the fact that the 3DOWC and 3DSBWC experienced a certain amount of fiber straightening and yarn waviness or consisted of Z-directional yarns that limited the crack propagation.

In terms of displacement, the largest deformation was seen in 3DSBWC. This was mainly due to the straightening of inner-curved fibers under tension and the restraining effect of heavy-yarn waviness on crack propagation during the loading process. Likewise, for the 3DOWC, the strengthening effect of Z-yarns on the Z-direction, results in high levels of deformation.

The 3DSSWC and 2D laminate underwent similar deformation (albeit with significantly lower magnitude, as the small degree of yarn buckling has almost no restraining effect on crack propagation) to that observed for 3DSSWC and 3DOWC. Therefore, since the small degree of yarn buckling can hardly prevent the crack propagation. Therefore, the coupons failed immediately upon crack initiation and thus the degree of deformation was small, as shown in Fig. 8.

The four composites can be ranked in descending order of the failure loads, i.e., 3DSBWC > 3DOWC > 3DSSWC > 2D laminate. The failure load of 3DSBWC was 1.75 times, 11.67 times, and 12 times that of 3DOWC, 3DSSWC, and 2D laminate, respectively. However, the four composites had a differing thickness (due to the structural influence) and, hence, stress analysis was required for a valid comparison of the results.

Consider a coupon subjected to a load F, which can be decomposed into a tensile load F_1 (perpendicular to the cross-section) and a tangential load F_2 (parallel to the cross-section). Based on the angle (θ, see Fig. 9) between F and F_2, the magnitude of F_1 and F_2 can be calculated from:

$$F_1 = F * \sin \theta \qquad (1)$$

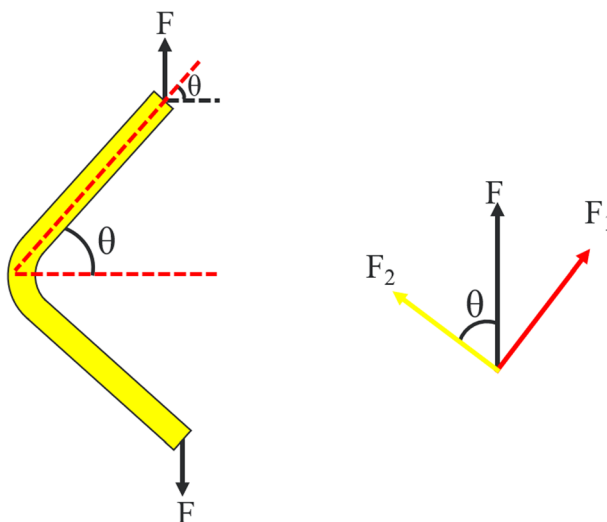$$F_2 = F * \cos \theta \qquad (2)$$

Fig. 9 Stress analysis for L-shape beam testing

Therefore, the normal stress induced by F1 and the shear stress induced by F2 can be calculated from Eqs. (3) and (4):

$$\sigma = F_1/(w*t) \tag{3}$$

$$\tau = \sigma/\tan\theta \tag{4}$$

Where, w and t are the width and thickness of the coupon, respectively.

The results revealed that the tensile strengths at failure in 2D laminate and 3DSSWC were basically the same (see Table 3), indicating that the poor delamination resistance of the 3DSSW structure associated with the L-shape beams. The tensile strengths at the failure of 3DOWC and 3DSBWC were significantly higher than those of 2D laminate and 3DSSWC. This indicated that the 3DOW and 3DSBW structures yielded a significant increase in the through-thickness reinforcement (3DSBW yielded a greater increase than 3DOW structure).

In conclusion, 3DOW and 3DSBW constructions yielded significant improvements in the Z-directional strength of the L-shape beams, especially in terms of the delamination resistance. However, compared with the 2D laminates, the 3DSSW structure had little improvement effect on the delamination resistance.

3.3 Failure Mode

The basis the above differences is determined by investigating the failure process and ultimate failure modes of L-shape composites composed of conventional 2D and three 3D woven composites.

3.3.1 2D Laminate L-shape Composite

The failure process of the 2D laminate L-shape beam is shown in Fig. 10a. Delamination started near the outer edge of the coupon and was accompanied by a slight drop in the load value, as shown in Fig. 10b ①. The sharp decrease in load (starting at the ② site) accompanying the increased in load, is attributed to the new delamination. The subsequently formed cracks spread rapidly along the weft direction at the edge of the specimen, leading eventually failure of the sample.

The X-ray CT scanning results of the tested coupon are shown in Fig. 11. As the figure shows, the a-a' section consisted of partial cracks only. This resulted mainly from the fact that crack widths lower than 7 μm scale exceed the detection limits. However, evidence of delamination was easily detected (see Fig. 10). In the b-b' section (see Fig. 11b), the cracks formed between the adjacent weft yarns and propagated along the weft direction without yarn breakage, indicating that the sample failure was dominated by interlayer delamination. The yarn waviness in the 2D laminate was small

Table 3 Results of the stress analysis

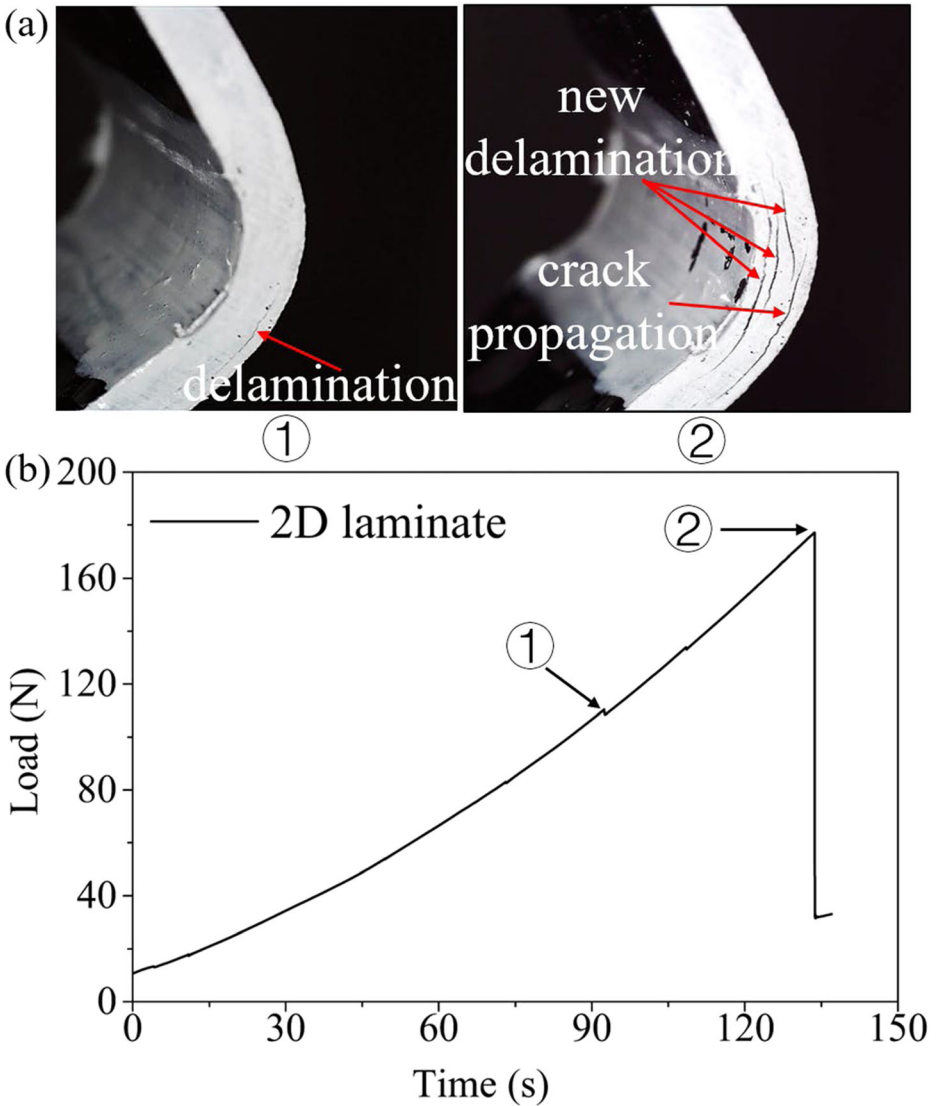| Structure	Load N	Angle θ	Normal stressF₁/N	Tensile strengthσ/MPa	Tangential strength τ/MPa
2D	156.3	47	114.3	3.4	3.2
3DSSW	285.5	50	232.4	3.5	2.9
3DOW	1885.4	51	1465.2	15.2	12.3
3DSBW	3221.6	52	2538.7	37.9	29.7

Fig. 10 Failure mode of the 2D laminate, **a** the damage morphology in ① and ②, **b** load -time curve
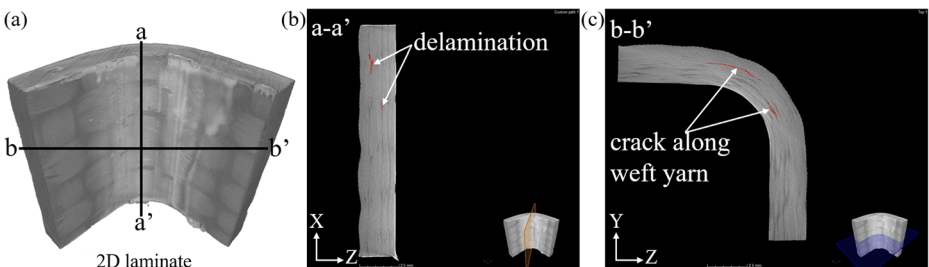

Fig. 11 **a** X-ray CT of 2D laminate and damage morphologies along the **b** a-a' direction and **c** b-b' direction of the 2D laminate
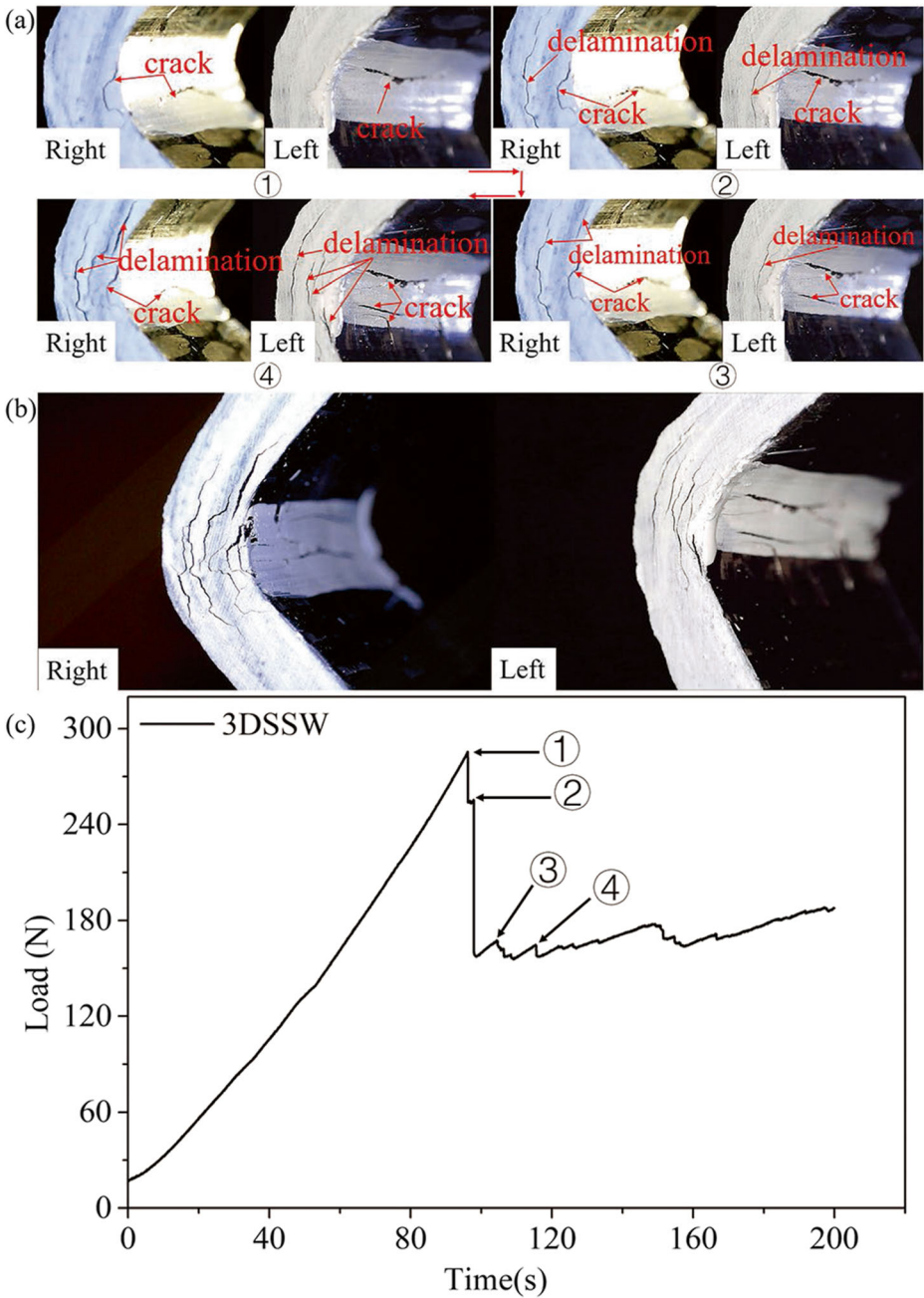
Fig. 12 The failure mode of 3DSSWC, **a** the damage morphology of the right and left sides of the sample in ①-④, **b** final failure mode and **c** load -time curve of 3DSSWC

and, hence, low amounts of energy were required for crack propagation. Therefore, the 2D laminate exhibited poor delamination resistance.
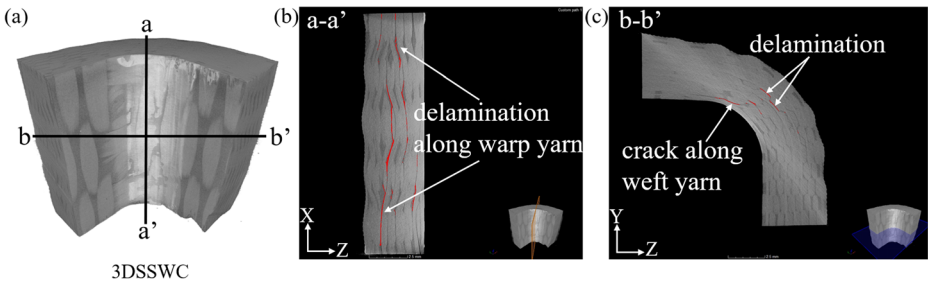
Fig. 13 **a** X-ray CT of 3DSSWC and damage morphologies along the **b** a-a' direction and **c** b-b' direction of 3DSSWC

The failure mode identified above concurs with the observed tensile strength of the 2D L-shape composite beams. This confirms that the 2D laminates failed mainly via the interlayer delamination resulting from the absence of fiber reinforcement in the Z-direction.

3.3.2 3DSSW L-shape Composite

Analysis of the failure process and load-time curve of 3DSSWC revealed that, during loading, cracks were simultaneously generated in the inner and outer edges of the specimen, as shown in Fig. 12a ①. Correspondingly, the load value decreased suddenly (see Fig. 12c ①). The load value increased (in general) at the ② site, but dropped instantly upon delamination, as shown in Fig. 12a ②.

Moreover, as additional load is applied, the number of cracks increased and these cracks extended rapidly along the weft direction (see Fig. 12a ③ and ④). The load value fluctuated slightly, as shown in Fig. 12c ③ and ④, and then the coupon failed (see in Fig. 12b).

The corresponding X-ray CT scanning results of 3DSSWC are shown in Fig. 13. In the a-a' section, the damage was initiated in the region where yarn crimping occurred, and then propagated along the warp direction (i.e., X-direction). This is attributed to the stress concentration associated with the region of yarn waviness, which resulted in interlayer delamination. In contrast, the yarn waviness in 3DSSWC was small and, hence, only a low amount of energy was required for crack propagation. This result in a sudden load drop upon crack initiation (see in Fig. 12c), indicating that the 3DSSWC exhibited poor delamination resistance, similar to that of the 2D laminates.

In the b-b' section, the cracks occurred between the fourth and fifth layers of the weft yarns where the material experienced the highest shear strength. Additionally, when the crack propagated along the weft direction, the main failure mode was dominated by the delamination between weft yarns and warp yarns. Therefore, the 3DSSW as a reinforcement structure yielded only modest improvements in the interlaminar strength of the composites.

The above failure analysis revealed that 2D laminate and 3DSSWC failed primarily via interlayer delamination, induced by the out-of-plane tensile stresses. Moreover, the subsequent crack propagation was interlaminar along both the weft and warp directions, without fiber damage prior to the delamination failure. This indicated that the interlaminar strength of 2D laminate and 3DSSWC is a function of the interlaminar strength characterizing the plies.

However, in terms of load attenuation and crack path, the 2D laminate failed immediately upon crack formation and the crack extended rapidly along the weft direction. The load-bearing capacity of 3DSSW remained at a certain level even for a load drop of 50% and crack propagation along the weft yarns yielded a zigzag pattern, as shown in Fig. 12b. Therefore,
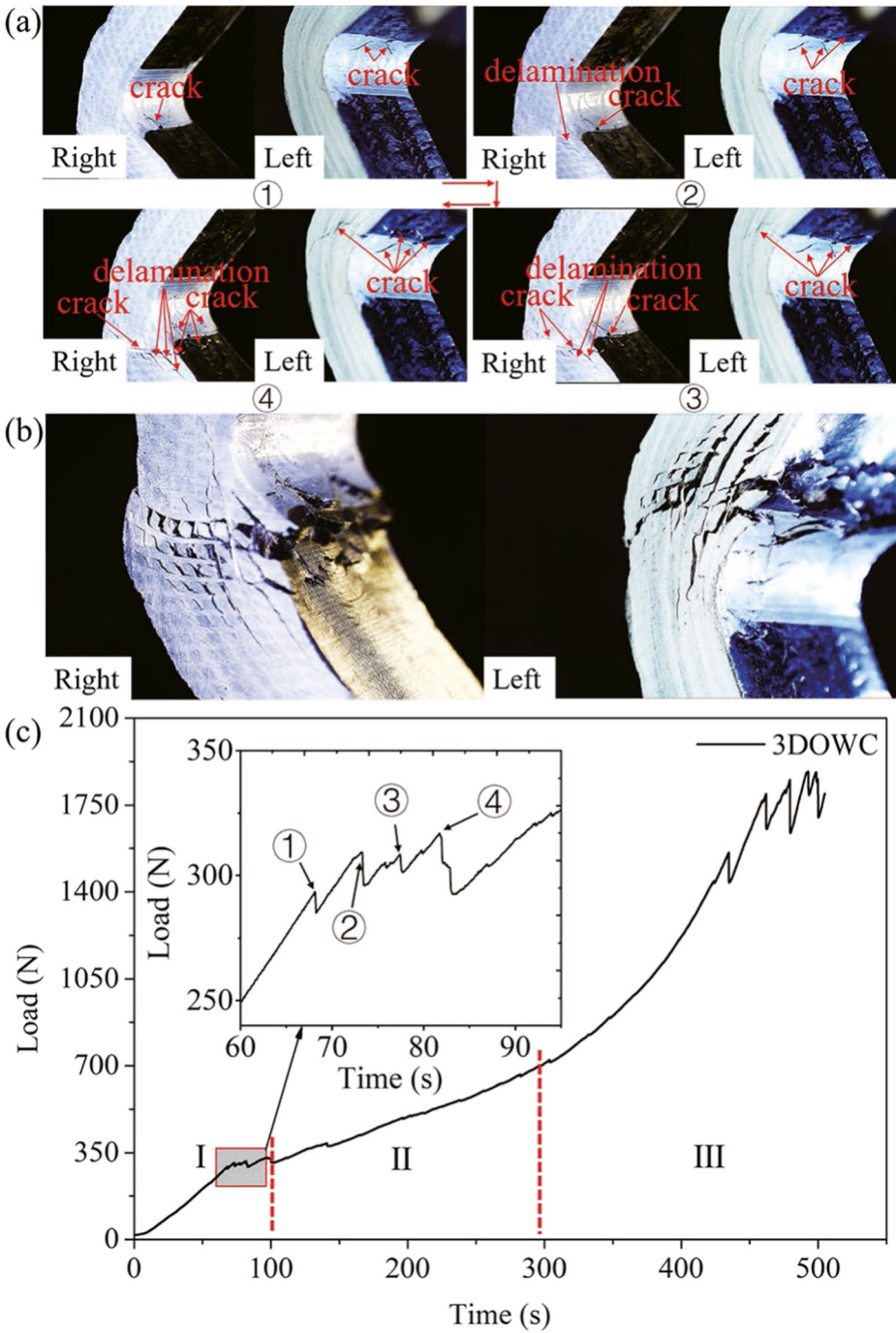
Fig. 14 Failure mode of 3DOWC, **a** the damage morphology of the right and left sides of the sample in ①-④, **b** final failure mode and **c** load -time curve of 3DOWC

compared with 2D laminate, the 3DSSWC exhibited a slightly higher delamination resistance and the 3DSSW structure had a slight strengthening effect on the interlaminar strength.

3.3.3 3DOW L-shape Composite

The tensile failure of 3DOWC is shown in Fig. 14a. A parabolically shaped crack, which was the same as the surface Z-yarn path, occurred on the inner surface of the coupon, as shown in Fig. 14a ①. Considering the slight drop in the load (see Fig. 14c ①), this crack may have resulted from the inner surface resin failure induced by the tensile circumferential stress during loading.

As the load continued to increase, new cracks were formed and delamination occurred at the inner face and the edge of the specimen, respectively (see Fig. 14a ②and③). However, the load drop (see Fig. 14c ②and③) was small, indicating that the damage may have resulted from debonding of the fiber and resin. The highest load drop (see in Fig. 14c ④) was attributed to an increase in both the crack number and width. These cracks propagated along the thickness and the arm direction, as shown in Fig. 14a ④.

Failure of the specimen was non-immediate, despite the formation and propagation of many cracks. In fact, the load and the slope of the curve both increased with further loading, indicating that the load carrier parts have changed. In region I, damage occurred mainly via delamination resulting from interlaminar shear (see Fig. 14c). Cracks propagation was subsequently hindered by the Z-yarns, leading to bearing by the Z-yarns and, in turn, failure upon breakage of these yarns. As a result, the load-bearing body changed from the interlaminar region to the Z-yarns and, hence, the slope of the curve increased in the region II, as shown in Fig. 14c.

Some of the Z-yarns failed in region II, resulting in load transfer to the weft yarns and, in turn, an increase in the slope of the curve in region III (see Fig. 14c). The weft yarns were subjected to two types of force during the loading: the inner weft yarns underwent tension and stretching, whereas the outer weft yarns underwent compression. Under these two forces, the weft yarns could fail either under tension or compression, and the cracks propagated along either the thickness or weft yarn direction. This resulted in delamination and breakage of the Z-yarns and weft yarns until failure of the coupon occurred, as shown in Fig. 14b.

The failure modes characterizing the 3DOWC differed significantly from those of the previous two composites (see Fig. 15). As the figure shows, delamination in the a-a' section occurred in the Z-yarn free region, i.e., the region between the warp yarns, and the cracks were only partly extended along these yarns. Z-yarn breakage also occurred in the a-a' section, indicating that crack propagation was hindered by the Z-yarns.
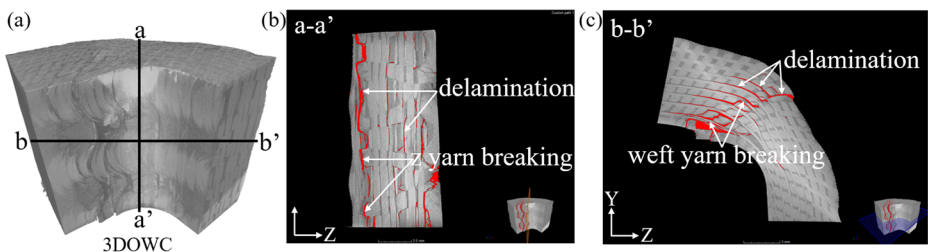

Fig. 15 **a** X-ray CT of 3DOWC and damage morphologies along the **b** a-a' direction and **c** b-b' direction of 3DOWC

However, cracks occurred between the adjacent warp yarns and extended along the weft yarns and Z-yarns, leading to the breakage of these yarns, as shown in Fig. 15b. As a result, the slope of the load-displacement curve increased in region III, as previous shown in Fig. 8.
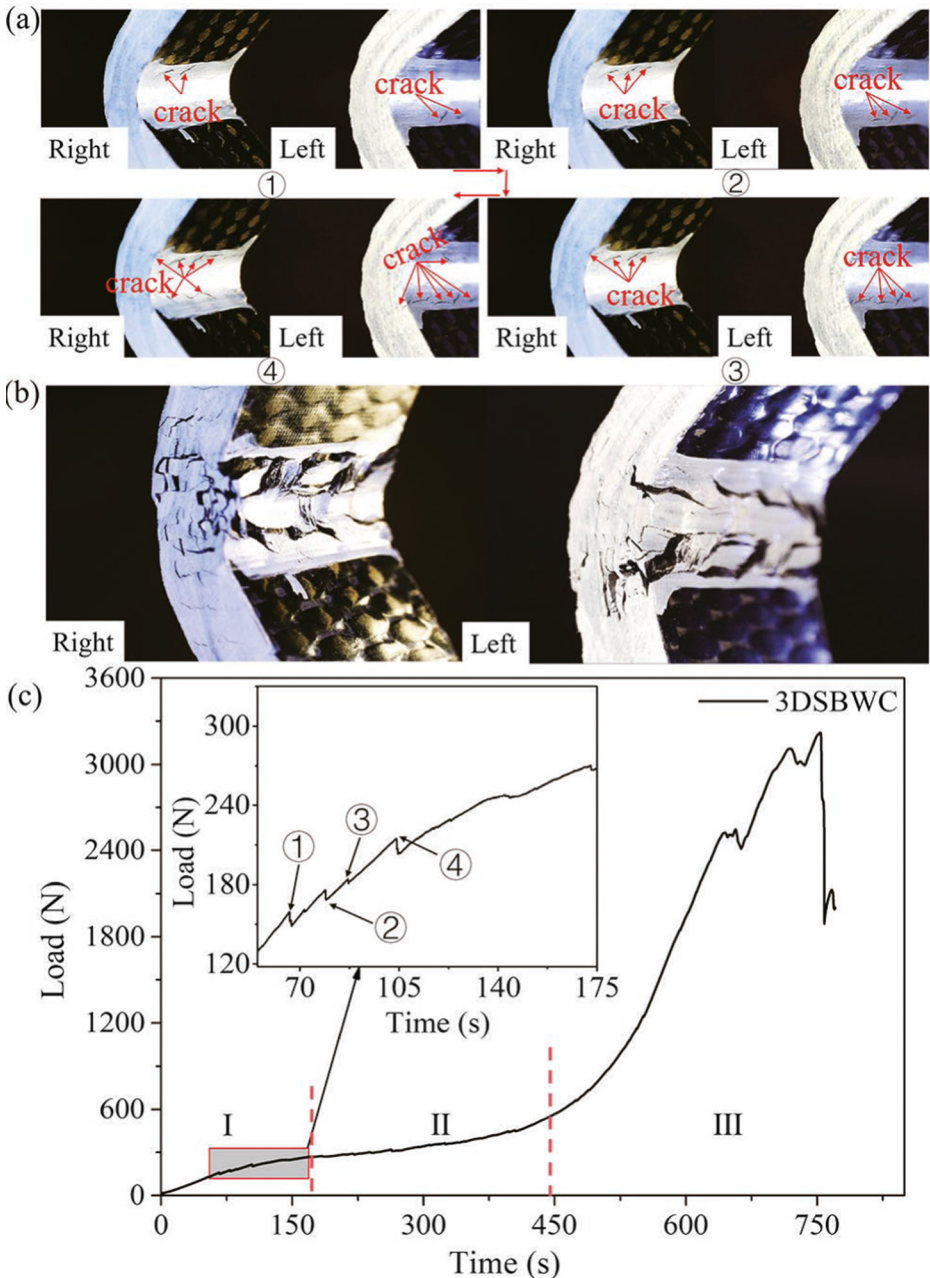

Fig. 16 Failure mode of 3DSBWC, **a** the damage morphology of the right and left sides of the sample in ①-④, **b** final failure mode and **c** load -time curve of 3DSBWC

To Summarize, the above failure process and failure mode analysis indicated that failure of the 3DOW L-shape composite beams under quasi-static tension can be divided into three stages. These stages were characterized by inner surface resin failure and delamination between yarns (first stage), yarn debonding and Z-yarn breakage during crack propagation (second stage), and Z-yarn as well as weft yarn breakage (stage three).

Therefore, owing to the reinforcing Z-yarns lying along the through-thickness direction of the 3DOWC, this material exhibited better delamination resistance than both the 2D laminate and 3DSSWC. In other words, compared with the 2D and 3DSSW structures, the 3DOW structure was more beneficial for resisting delamination.

3.3.4 3DSBW L-shape Composite

In the case of the 3DSBW L-shape composite, cracks formed preferentially at the inner surface of the coupon, as shown in Fig. 16a ①. Nonetheless, the low load value and the slight load drop, shown in Fig. 16c ①, indicated that crack formation was probably initiated at the inner radius surface-resin damage resulting from the tensile circumferential stress. With this slight drop in load, subsequent cracks (shown in Fig. 16a ②and③) also started at and extended from the inner radius surface. This suggested that the main damage was dominated via fiber-resin debonding and resin-crack formation. However, the number of cracks increased sharply and these cracks propagated through the thickness (see Fig. 16a ④), indicating that the load bore elements were changed gradually from the resin interlayer to the fibers.

However, the load value increased gradually during subsequent loading, and a yield point occurred in the 2–7 mm region, as previously shown in Fig. 8. This resulted from the fact that failure in this region occurred mainly via delamination and fiber straightening damage. Nevertheless, the slope of the load-displacement curve increased rapidly in subsequent regions, indicating that the fibers started to bear the load and the failure mode was dominated by fiber tensile failure. This could also be seen in the final failure shown in Fig. 16b.

Similarly, the failure mode in a-a' section, shown in Fig. 17a, was dominated by delamination, confirming that the 3DSBWC had a yield point at displacements of 2–7 mm (see Fig. 8). In the b-b' section, the cracks propagated along the weft yarns. Some of these yarns were damaged by tension or compression, indicating that the failure mode had changed from delamination to the breakage of weft yarns. This was evidenced by the sudden increase in the slope of the load-displacement curve.

Therefore, the failure of the 3DSBWC occurred in three stages. The first stage was dominated by cracking of the inner radius surface resin, as well as debonding of fiber and resin. The second stage was characterized by interlaminar delamination and fiber stretching,
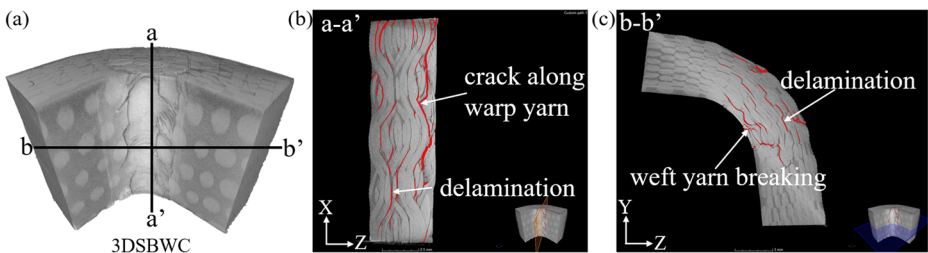

Fig. 17 **a** X-ray CT of 3DSBWC and damage morphologies along the **b** a-a' direction and **c** b-b' direction of 3DSBWC

whereas the third stage was characterized by fiber tension failure. The failure process also showed that the 3DSBWC had the ability to carry significant loads even after initial failure had occurred and progressed to other areas.

The bearing capacity and the ultimate tensile strength of the 3DSBWC were both considerably higher than those of 3DOWC, and the corresponding L-beam exhibited the highest delamination resistance among the four structures. This resulted from the inclination of the Z-yarns comprising 3DOWC, this inclination led to a significant reduction in the contribution of 3DOWC to the Z-directional tensile strength.

In summary, a sharp drop in the load value and coupon delamination failure occurred in the 2D and 3DSSW L-shape composites where cracks resulted from a small yarn waviness and an absence of fibers in the Z-direction. In contrast, for 3DOWC and 3DSBWC, cracks formed first at the inner radius (due to the circumferential tensile stress) and then propagated across the entire width and thickness of the specimen. Subsequent crack propagation to the fibers, resulted in a high tensile strength.

Therefore, the 3DOWC and 3DSBWC exhibited significantly higher delamination resistance than the 2D laminate and 3DSSWC. Moreover, owing to the inclination of the constituent Z-yarns, the delamination resistance of 3DOWC is lower than that of 3DSBWC and, hence, the 3DSBWC L-shape beam exhibited the best delamination resistance of the four composites.

4 Conclusion

The effect of reinforcement structures (i.e., 2D, 3DSSW, 3DOW, 3DSBW) on the load-bearing capability and failure mode of L-shape composite beams was investigated via hinged loading tensile tests and Micro-X-CT.

Failure mode analysis of the four composites, revealed that the 2D laminate and 3DSSWC underwent (mainly) interlayer delamination (owing to the out-of-plane tensile stress) accompanied by a sharp drop in the load value and failure of the coupon. This was attributed to the lack of reinforcing fibers in the Z-direction of the 2D composites, and crimping of the small yarns (for interlaminar reinforcement) in 3DSSWC. In other words, the interlaminar strength was decided by the fiber-resin interfacial and, therefore, the primary failure mode in 2D laminate and 3DSSWC was delamination. However, interlayer delamination in 3DOWC was restrained, owing to the presence of reinforcing through-thickness Z-yarn fibers. The failure mode in 3DOWC was therefore characterized by the delamination between the warp and weft yarns in Z-yarn free regions, as well as the breakage of both yarn types. Although the interlaminar strength of 3DSBWC was also decided by the yarn waviness, the yarn crimping was more severe in 3DSBWC than in 3DSSWC. Crack propagation in 3DSBWC, therefore, required more energy than propagation in 3DSSWC. The final failure mode of 3DSBWC was characterized by interlayer delamination, together with weft yarn tension or compression breakage.

Therefore, the delamination resistance of 3DOWC and 3DSBWC was higher than that of 2D laminate and 3DSSWC. However, owing to the inclination of the Z-yarns in the 3DOWC, the Z-yarn contribution to the interlaminar strength was extremely limited and, hence, the tensile strength of 3DOWC was lower than that of 3DSBWC. The 3DOW and 3DSBW reinforced L-shape composites, compared with 2D and 3DSSW, yielded superior delamination resistance, rendering these the structures ideal for reinforcement ribs, spars and primary load-bearing structures.

References

1. Mouritz, A.P., Bannister, M.K., Falzon, P.J., Leong, K.H.: Review of applications for advanced three-dimensional fibre textile composites. Composites Part A Applied Science & Manufacturing. **30**(12), 1445–1461 (1999)
2. Mair, R.I.: Advanced composite structures research in Australia. Compos. Struct. **57**(1–4), 3–10 (2002)
3. Guess, T.R., Reedy, E.D.: Interlocked fabric and laminated fabric Kevlar 49/epoxy composites. No. SAND-88-2579C; CONF-8810151-4. Sandia National Labs., Albuquerque (1988)
4. Behera, B.K., Dash, B.P.: Mechanical behavior of 3D woven composites. Mater. Des. **67**, 261–271 (2015)
5. Aiman, D.P.C., Yahya, M.F., Salleh, J.: Impact properties of 2D and 3D woven composites : a review. In: AIP Conference Proceedings, pp. 020002 (2016)
6. Stig, F., Hallström, S.: Assessment of the mechanical properties of a new 3D woven fibre composite material. Compos. Sci. Technol. **69**(11–12), 1686–1692 (2009)
7. Turner, P., Liu, T., Zeng, X.: Collapse of 3D orthogonal woven carbon fibre composites under in-plane tension/compression and out-of-plane bending. Compos. Struct. **142**, 286–297 (2016)
8. Luo, Y., Lv, L., Sun, B., Qiu, Y., Gu, B.: Transverse impact behavior and energy absorption of three-dimensional orthogonal hybrid woven composites. Compos. Struct. **81**(2), 202–209 (2007)
9. Turner, P., Liu, T., Zeng, X., Brown, K.: Three-dimensional woven carbon fibre polymer composite beams and plates under ballistic impact. Compos. Struct. **185**, 483–495 (2018)
10. Hiel, C.C., Sumich, M., Chappell, D.P., Curved Beam, A.: Test specimen for determining the interlaminar tensile strength of a laminated composite. J. Compos. Mater. **25**(7), 854–868 (1991)
11. Martin, R.H., Jackson, W.C.: Damage prediction in cross-plied curved composite laminates. Composite materials: fatigue and fracture, vol. 4. ASTM International, Philadephia (1991)
12. Martin, R.H.: Delamination failure in a unidirectional curved composite laminate. Composite materials testing & design, vol. 10. ASTM International, Philadephia (1992)
13. Gözlüklü, B., Coker, D.: Modeling of the dynamic delamination of L-shaped unidirectional laminated composites. Compos. Struct. **94**(4), 1430–1442 (2012)
14. Jackson, W. C, Portanova, M.A: Out-Of-Plane Properties. In: Mechanics of Textile Composites Conference. NASA-CP3311, part 2, pp. 315–348 (1995)
15. Jackson, W.C., Ifju, P.G.: Through-the-thickness tensile strength of textile composites. Composite materials: testing and design, vol. 12, pp. 218–238. ASTM International, Philadephia (1994)
16. Martin, R.H., Jackson, W.C.: An interlaminar tensile strength specimen. Composite materials—testing and design, vol. 11. ASTM International, Philadephia (1993)
17. Wimmer, G., Kitzmüller, W., Pinter, G., Wettemann, T., Pettermann, H.E.: Computational and experimental investigation of delamination in L-shaped laminated composite components. Eng. Fract. Mech. **76**(18), 2810–2820 (2009)
18. Yavas, D., Gozluklu, B., Coker, D.: Investigation of Crack Growth along Curved Interfaces in L-Shaped Composite and Polymers. Springer International Publishing (2014)
19. Gozluklu, B., Uyar, I., Coker, D.: Intersonic delamination in curved thick composite laminates under quasi-static loading. Mech. Mater. **80**, 163–182 (2015)
20. Uyar, I., Gozluklu, B., Coker, D.: Dynamic delamination in curved composite laminates under quasi-static loading. J. Phys. Conf. Ser. **524**, Artn 012042 (2014). https://doi.org/10.1088/1742-6596/524/1/012042
21. Uyar, I., Arca, M.A., Gozluklu, B., Coker, D.: Experimental observations of dynamic delamination in curved [0] and [0/90] composite laminates. Fracture, fatigue, failure, and damage evolution, vol. 5, pp. 189–196. Springer, Cham (2015)
22. Arca, M.A., Papila, M., Coker, D.: Experimental investigation of strength of curved beam by thin ply non-crimp fabric laminates. Fracture, fatigue, failure and damage evolution, vol. 8, pp. 37–42. Springer, Cham (2017)
23. Redman, C., Bayraktar, H., Mcclain, M.: Curved beam test behavior of 3D woven composites. In: SAMPE 2014, International SAMPE Symposium and Exhibition, Seattle. Society for the Advancement of Material and Process Engineering (SAMPE), Covina (2014)
24. Chen, B., Chou, T.W.: Compaction of woven-fabric preforms in liquid composite molding processes: single-layer deformation. Compos. Sci. Technol. **59**(10), 1519–1526 (1999)

25. Saunders, R.A., Lekakou, C., Bader, M.G.: Compression and microstructure of fibre plain woven cloths in the processing of polymer composites. Composites Part A Applied Science & Manufacturing. **29**(4), 443–454 (1998)
26. Chen, B., Lang, E.J., Chou, T.W.: Experimental and theoretical studies of fabric compaction behavior in resin transfer molding 1. Mater Sci Eng A. **317**(1–2), 188–196 (2001)
27. Potluri, P., Sagar, T.V.: Compaction modelling of textile preforms for composite structures. Compos. Struct. **86**(1–3), 177–185 (2008)
28. Green, S.D., Long, A.C., Said, B.S.F.E., Hallett, S.R.: Numerical modelling of 3D woven preform deformations. Compos. Struct. **108**(1), 747–756 (2014)
29. Vernet, N., Trochu, F.: Analysis and modeling of 3D interlock fabric compaction behavior. Composites Part A. **80**, 182–193 (2016)